

## Concentration-gradient Prussian blue cathodes for Na-ion batteries

Pu Hu, Wenbo Peng, Bo Wang, Dongdong Xiao, Utkarsh Ahuja, Julien Réthoré, and Katerina Aifantis

*ACS Energy Lett.*, **Just Accepted Manuscript** • DOI: 10.1021/acsenergylett.9b02410 • Publication Date (Web): 25 Nov 2019

Downloaded from [pubs.acs.org](https://pubs.acs.org) on November 26, 2019

### Just Accepted

“Just Accepted” manuscripts have been peer-reviewed and accepted for publication. They are posted online prior to technical editing, formatting for publication and author proofing. The American Chemical Society provides “Just Accepted” as a service to the research community to expedite the dissemination of scientific material as soon as possible after acceptance. “Just Accepted” manuscripts appear in full in PDF format accompanied by an HTML abstract. “Just Accepted” manuscripts have been fully peer reviewed, but should not be considered the official version of record. They are citable by the Digital Object Identifier (DOI®). “Just Accepted” is an optional service offered to authors. Therefore, the “Just Accepted” Web site may not include all articles that will be published in the journal. After a manuscript is technically edited and formatted, it will be removed from the “Just Accepted” Web site and published as an ASAP article. Note that technical editing may introduce minor changes to the manuscript text and/or graphics which could affect content, and all legal disclaimers and ethical guidelines that apply to the journal pertain. ACS cannot be held responsible for errors or consequences arising from the use of information contained in these “Just Accepted” manuscripts.

1  
2  
3  
4  
5  
6  
7  
8  
9  
10  
11  
12  
13  
14  
15  
16  
17  
18  
19  
20  
21  
22  
23  
24  
25  
26  
27  
28  
29  
30  
31  
32  
33  
34  
35  
36  
37  
38  
39  
40  
41  
42  
43  
44  
45  
46  
47  
48  
49  
50  
51  
52  
53  
54  
55  
56  
57  
58  
59  
60

# Concentration-gradient Prussian blue cathodes for Na-ion batteries

*Pu Hu,† Wenbo Peng,† Bo Wang,† Dongdong Xiao,‡ Utkarsh Ahuja,† Julien Réthoré,§ and Katerina E. Aifantis,\*†*

† Department of Mechanical and Aerospace Engineering, University of Florida,  
Gainesville, 32603, USA

‡ Beijing National Laboratory for Condensed Matter Physics, Institute of Physics,  
Chinese Academy of Sciences, Beijing 100190, China

§ Research Institute in Civil and Mechanical Engineering (Gem), CNRS UMR 6183  
CNRS / Ecole Centrale de Nantes / Université de Nantes, F-44 321, Nantes, France.

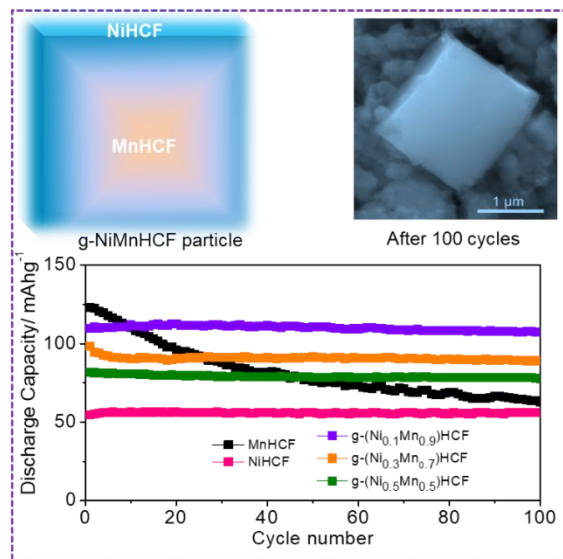
AUTHOR INFORMATION

**Corresponding Author**

1  
2  
3 \* Email: kaifantis@ufl.edu  
4  
5  
6  
7

8 ABSTRACT A concentration-gradient composition is proposed as an effective approach  
9  
10  
11 to solve the mechanical degradation and improve the electrochemical cyclability for  
12  
13 cathodes of sodium-ion batteries. Concentration-gradient shell  $\text{Na}_x\text{Ni}_y\text{Mn}_{1-y}\text{Fe}(\text{CN})_6 \cdot n\text{H}_2\text{O}$ ,  
14  
15 in which the Ni content gradually increases from the interior to the particle surface, is  
16  
17 synthesized by a facile co-precipitation process. The as-obtained cathode exhibits an  
18  
19 improved electrochemical performance compared to homogeneous  $\text{Na}_x\text{MnFe}(\text{CN})_6 \cdot n\text{H}_2\text{O}$ ,  
20  
21 delivering a high reversible specific capacity of  $110 \text{ mA h g}^{-1}$  at 0.2 C and outstanding  
22  
23 cycling stability (93% retention after 1000 cycles at 5 C). The improvement of  
24  
25 electrochemical performance can be attributed to its robust microstructure that effectively  
26  
27 alleviates the electrochemically induced stresses and accumulated damage during  
28  
29 sodiation/desodiation and thus prevents the initiation of fracture in the particles upon long  
30  
31 term cycling. These findings render a prospective strategy to develop high-performance  
32  
33 electrode materials for sodium-ion batteries.  
34  
35  
36  
37  
38  
39  
40  
41  
42  
43  
44  
45  
46  
47  
48  
49  
50  
51

52  
53  
54  
55 **TOC GRAPHICS**  
56  
57  
58  
59  
60



Sodium ion batteries (SIBs) have been gaining increased attention as a potential energy storage device.<sup>1-4</sup> Compared to lithium, sodium is available abundantly and relatively inexpensive, thereby reducing the cost of the electrode material. Moreover, sodium has similar electrochemical properties to lithium and maintains a good reversibility in a variety of host materials. Hence, significant efforts are being undertaken to commercialize SIBs for large-scale energy storage (EES) systems. Recently, a SIBs system with a power rating of 30 kW/100 kWh was installed in China.<sup>5</sup> Nevertheless, long-term cycling stability of SIBs still remains a challenge.

1  
2  
3  
4 Mechanical degradation is commonly observed in both cathode and anode materials  
5  
6  
7 of Li-ion batteries, which is the leading contributor of capacity decay of batteries.<sup>6-10</sup>  
8  
9  
10 Fracture of the electrodes is caused by volume expansions, phase transformations,  
11  
12  
13 formation of oxygen vacancies and surface corrosion of the active materials upon  
14  
15  
16 intercalation.<sup>11-14</sup> Such mechanisms have been experimentally observed in cathode  
17  
18  
19 materials ( $\text{LiNi}_{1/3}\text{Mn}_{1/3}\text{Co}_{1/3}\text{O}_2$ ,  $\text{LiMn}_2\text{O}_4$ ,  $\text{LiFePO}_4$ ) for LIBs,<sup>14-16</sup> and although their  
20  
21  
22 volumetric expansions are less than 10% (2.0% expansion along c direction for  
23  
24  
25  $\text{LiNi}_{1/3}\text{Mn}_{1/3}\text{Co}_{1/3}\text{O}_2$ <sup>17</sup>, 7% expansion for  $\text{LiFePO}_4$ <sup>18</sup>, and 6.77% expansion for  $\text{LiFePO}_4$ <sup>19</sup>),  
26  
27  
28 repeated lattice expansion and contraction during electrochemical cycling leads to  
29  
30  
31 accumulation of damage which subsequently leads to mechanical degradation of the  
32  
33  
34 electrode. Due to the larger ionic radius of  $\text{Na}^+$  from  $\text{Li}^+$ , the electrode during  
35  
36  
37 sodiation/desodiation is subjected to larger volumetric strains and more complicated  
38  
39  
40 multi-phase transformations than those during lithiation/delithiation.<sup>20-21</sup> This suggests  
41  
42  
43 that mechanical degradation may result in more severe damage in cathode materials  
44  
45  
46 during the charge/discharge process in SIBs. Our previous research revealed that the  
47  
48  
49 maximum effective von Mises stress in a layered-type  $\text{TiS}_2$  cathode was four times higher  
50  
51  
52  
53  
54  
55  
56  
57  
58  
59  
60

1  
2  
3 during sodiation than lithiation and numerous cracks were observed with electron  
4  
5  
6  
7 microscopy after continuous electrochemical cycling. Therefore, understanding the  
8  
9  
10 mechanical degradation as well as (de)sodiation-induced fracture of cathodes is essential  
11  
12  
13 in achieving long-term stability in SIBs. To date, a systematic investigation on the effect  
14  
15  
16 of the cathode mechanical properties to the electrochemical performance of SIBs is  
17  
18  
19 lacking.  
20  
21  
22  
23  
24

25 Prussian blue and its analogues (PBAs) with a unique 3D open-framework are  
26  
27  
28 promising cathode materials for SIBs.<sup>22-24</sup> These materials have a general formula of  
29  
30  
31  $A_xM_yFe(CN)_6 \cdot nH_2O$ , abbreviated as MHCF, (A is the alkali cation and M is a divalent or  
32  
33  
34 trivalent transition metal), in which six-fold C-coordinated Fe and six-fold N-coordinated  
35  
36  
37 M are connected by CN ligands, forming Fe–C≡N–M linked open-frameworks and large  
38  
39  
40 interstitial sites. The wide channels and weak interaction between the Na<sup>+</sup> ion and the  
41  
42  
43 cyanide triple bonds in such a unique structure allows fast Na<sup>+</sup> diffusion. Among PBAs,  
44  
45  
46 Na<sub>x</sub>MnFe(CN)<sub>6</sub> (MnHCF) exhibits a high redox potential and high theoretical capacity of  
47  
48  
49  
50 171 mAh/g, which is comparable to commercial LiFePO<sub>4</sub> cathodes in LIBs.<sup>25-28</sup> However,  
51  
52  
53  
54  
55  
56  
57  
58  
59  
60

1  
2  
3 a capacity decay is observed experimentally, as previous reports<sup>29-31</sup> show that only a  
4  
5  
6  
7 30% capacity retention is achieved after 200 cycles at 0.5 C in liquid electrolyte, which  
8  
9  
10 has been attributed to structural instabilities that take place during electrochemical  
11  
12  
13 cycling. Participation of both Fe and Mn sites in redox reactions results in lattice distortion  
14  
15  
16 and changes the C≡N bond length. Moreover, the structural instability of MnHCF is also  
17  
18  
19 caused by the crystal Jahn-Teller (J-T) distortion of Mn<sup>3+</sup> ( $t_{2g}^3e_g^1$ )<sup>32</sup> and volume changes  
20  
21 (~8.5%)<sup>31</sup> during cycling. In addition to structural changes, dissolution of Mn species in  
22  
23  
24 the organic electrolyte leads to surface corrosion of the electrode.<sup>29</sup> All these factors  
25  
26  
27 would be expected to contribute to local fracture and mechanical degradation of the PBA  
28  
29  
30 electrode, leading to capacity decay. It is known that Ni<sup>2+</sup> is electrochemically inert in  
31  
32  
33 Na<sub>2</sub>NiFe(CN)<sub>6</sub> (NiHCF) and Fe is the only redox active site, making the Fe–C≡N–Ni bond  
34  
35 extremely stable. Earlier studies have shown that NiHCF undergoes zero lattice strain (volume  
36  
37 change ~ 0.29%) during sodiation/desodiation and displays excellent cycling stability (90%  
38  
39 capacity retention over 1000 cycles).<sup>27</sup>  
40  
41  
42  
43  
44  
45  
46  
47

48 In the present study a concentration-gradient composition is proposed as an effective  
49  
50  
51 approach to solve the mechanical degradation and improve the electrochemical cyclability  
52  
53  
54 for cathodes of sodium-ion batteries. Concentration-gradient Na<sub>x</sub>Ni<sub>y</sub>Mn<sub>1-y</sub>Fe(CN)<sub>6</sub>·nH<sub>2</sub>O  
55  
56  
57  
58  
59  
60

1  
2  
3  
4 (g-Na<sub>x</sub>Ni<sub>y</sub>Mn<sub>1-y</sub>Fe(CN)<sub>6</sub>·nH<sub>2</sub>O), in which Ni gradually increases while Mn decreases from  
5  
6  
7 the interior to the particle surface, is synthesized by a facile co-precipitation process. The  
8  
9  
10 NiHCF shell does not experience volume changes upon sodiation and was anticipated to  
11  
12  
13 increase the mechanical stability of the MnHCF rich core that undergoes volume changes  
14  
15  
16 upon cycling. Phase field modelling is employed to capture the internal stresses  
17  
18  
19 developed during cycling and correlate mechanical with electrochemical stability. In  
20  
21  
22  
23 addition to testing the performance of these PBA materials in a half cell, a full cell was  
24  
25  
26  
27  
28 also fabricated and tested using either graphite or TiS<sub>2</sub> as the anode.  
29  
30  
31  
32  
33  
34  
35  
36  
37  
38  
39  
40  
41  
42  
43  
44  
45  
46  
47  
48  
49  
50  
51  
52  
53  
54  
55  
56  
57  
58  
59  
60

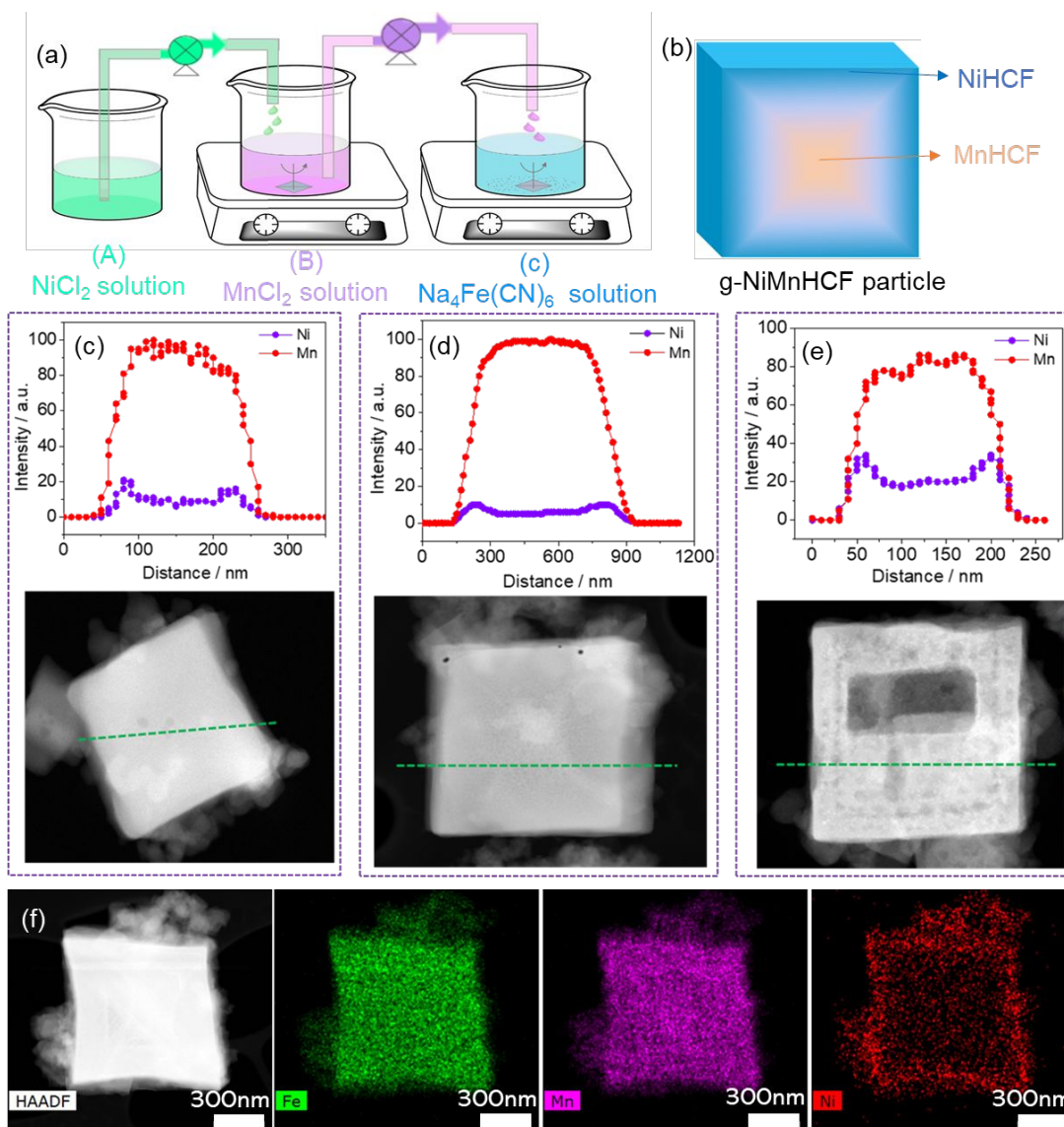


**Figure 1** (a) Schematics illustrating the preparation of g-NiMnHCF. (b) Illustration of a gradient particle, where NiHCF gradually increases while MnHCF decreases from the interior to the particle surface, forming a core/shell structure. (c)-(e) STEM images and EDX linear scan for the typical gradient particles with different Ni/Mn ratios: (c) g-

1  
2  
3  
4 (Ni<sub>0.1</sub>Mn<sub>0.9</sub>)HCF, (d) g-(Ni<sub>0.3</sub>Mn<sub>0.7</sub>)HCF and (e) g-(Ni<sub>0.5</sub>Mn<sub>0.5</sub>)HCF. (f) STEM images and  
5  
6  
7 element mapping for g-(Ni<sub>0.3</sub>Mn<sub>0.7</sub>)HCF.  
8  
9

10  
11 Concentration-gradient particles of g-(NiMn)HCF were prepared via a scalable co-  
12  
13 precipitation process, as described in **Figure 1a**. Ni<sup>2+</sup> solution was slowly pumped into the  
14  
15 Mn<sup>2+</sup> to obtain a mixture with increasing Ni<sup>2+</sup> concentration. The resultant mixture of  
16  
17 Ni<sup>2+</sup>/Mn<sup>2+</sup> was precisely pumped into Na<sub>4</sub>Fe(CN)<sub>6</sub> solution to form a precipitate under  
18  
19 constant magnetic stirring. As a result, concentration-gradient particles with a Ni-rich  
20  
21 surface and Mn-rich core were obtained (Figure1b). By adjusting the molar ratio of Ni<sup>2+</sup>  
22  
23 and Mn<sup>2+</sup> (1:9, 3:7, 1:1), a series of gradient Na<sub>x</sub>(Ni<sub>y</sub>Mn<sub>z</sub>)HCF with different  
24  
25 stoichiometries were synthesized. Thermogravimetric analysis (TGA) (Figure S1) and  
26  
27 ICP-OES (Table.S1) were carried out to determine the composition of the obtained  
28  
29 materials, which were identified as Na<sub>1.17</sub>(Ni<sub>0.12</sub>Mn<sub>0.88</sub>)[Fe(CN)<sub>6</sub>]<sub>0.79</sub>·1.5H<sub>2</sub>O,  
30  
31 Na<sub>1.37</sub>(Ni<sub>0.28</sub>Mn<sub>0.72</sub>)[Fe(CN)<sub>6</sub>]<sub>0.84</sub>·2.39H<sub>2</sub>O and Na<sub>1.81</sub>(Ni<sub>0.59</sub>Mn<sub>0.41</sub>)[Fe(CN)<sub>6</sub>]<sub>0.95</sub>·3.3H<sub>2</sub>O.  
32  
33  
34  
35  
36  
37  
38  
39  
40  
41  
42  
43  
44  
45  
46  
47  
48  
49  
50 The molar ratio of Ni/Mn in these materials was found to be close to the molar ratio of  
51  
52 Ni<sup>2+</sup>/Mn<sup>2+</sup> mixture used in the synthesis. We denoted them as g-(Ni<sub>0.1</sub>Mn<sub>0.9</sub>)HCF, g-  
53  
54  
55  
56  
57  
58  
59  
60

1  
2  
3  
4 (Ni<sub>0.3</sub>Mn<sub>0.7</sub>)HCF and g-(Ni<sub>0.5</sub>Mn<sub>0.5</sub>)HCF. Figure S2 shows the X-ray diffraction (XRD)  
5  
6  
7 patterns of the gradient materials as well as the homogeneous MnHCF and NiHCF. The  
8  
9  
10 splitting diffraction peaks for MnHCF at around 23.7° and 37.9° are a notable  
11  
12  
13 characteristic of monoclinic phases (P2<sub>1</sub>/n space group). From MnHCF to NiHCF, the  
14  
15  
16 diffraction peak shifted to a higher angle with increasing the Ni content in the materials.  
17  
18  
19 This is due to the radius of Ni<sup>2+</sup> (0.69Å) being smaller than that of Mn<sup>2+</sup>(0.83Å), leading to  
20  
21  
22 the shrinkage of the lattice for compounds with higher Ni contents. Fourier-transform  
23  
24  
25 infrared spectroscopy (FTIR) was performed to probe the chemical structure of the  
26  
27  
28 obtained materials. The absorption peak at 2085 cm<sup>-1</sup> in FTIR (Figure S3) revealed the  
29  
30  
31 characteristic stretching vibration of the cyanide (Fe–C≡N–M, M=Mn, Ni) group. Since the  
32  
33  
34 electronegativity of Ni (1.91) is higher than Mn (1.55), the substitution of Ni with Mn could  
35  
36  
37 induce an inductive effect, which lead to the blue shift of the peak. With increasing the Ni  
38  
39  
40  
41  
42  
43  
44  
45  
46  
47  
48  
49 concentration, the absorption peak gradually shifted to a higher wavenumber.

50 Scanning transmission electron microscopy (STEM) was carried out to determine the  
51  
52  
53 local composition and distribution of transition metals within a single particle. All the  
54  
55  
56  
57  
58  
59  
60

1  
2  
3 particles displayed a typical cubic nanostructure. Figure 1c-e shows the EDS (electron  
4  
5  
6  
7 diffraction spectroscopy) line scan and the corresponding STEM images of g-  
8  
9  
10  $(\text{Ni}_{0.1}\text{Mn}_{0.9})\text{HCF}$  (Figure 1c),  $\text{g}-(\text{Ni}_{0.3}\text{Mn}_{0.7})\text{HCF}$  (Figure 1d) and  $\text{g}-(\text{Ni}_{0.5}\text{Mn}_{0.5})\text{HCF}$  (Figure  
11  
12  
13  
14 1e) particles. The results reveal that all samples display the similar trend of distribution of  
15  
16  
17 Ni and Mn in the particle, where the Ni concentration increases gradually from the center  
18  
19  
20 towards the surface, and the Mn concentration is low on the surface but increases near  
21  
22  
23 the center of the particle. The gradient distribution of the transition metal in the particle is  
24  
25  
26 further confirmed by EDS element mapping (Figure 1f, Figure S4). Compared with the  
27  
28  
29  
30  
31 homogeneous distribution of Fe, the Ni and Mn are heterogeneously distributed between  
32  
33  
34 the center and surface. However, the intensity ratio of Ni/Mn is different from the designed  
35  
36  
37 ratio and the ICP-OES results. It might be due to the different solubility between  $\text{MnHCF}$  ( $K_{\text{sp}} \sim$   
38  
39  $10^{-3}$ ) and  $\text{NiHCF}$  ( $K_{\text{sp}} \sim 10^{-16}$ ), leading to the formation of  $\text{NiHCF}$  particles that mixed with the  
40  
41  
42 gradient materials. As shown in Figure S5,  $\text{g}-(\text{Ni}_{0.1}\text{Mn}_{0.9})\text{HCF}$  comprises of microcubes of similar  
43  
44  
45 sizes. STEM images and the corresponding linear scan results of homogeneous  $(\text{Ni}_{0.1}\text{Mn}_{0.9})\text{HCF}$   
46  
47  
48 and  $(\text{Ni}_{0.3}\text{Mn}_{0.7})\text{HCF}$  samples are shown in Figure S6, in which Ni, Fe and Mn elements exhibit a  
49  
50  
51 flat intensity along the linear scan, indicating the homogenous distribution of element from inner  
52  
53  
54 to the surface. These observations confirm that the synthesis method employed here can be applied  
55  
56  
57 to a wide range of Ni:Mn compounds to form a gradient particle with a controllable composition.  
58  
59  
60

1  
2  
3  
4 **Figure 2** compares the electrochemical performance of gradient composites with  
5  
6  
7 different Ni:Mn ratios and the homogeneous phase of MnHCF and NiHCF in Na half-cells.  
8

9  
10 Figure 2a shows the initial galvanostatic charge/discharge voltage profile of cycled cells  
11  
12  
13  
14 at 0.2 C. NiHCF displays a voltage plateau at ~ 3.4 V during charge and ~ 3.2 V during  
15  
16  
17 discharge, which is associated with the redox reaction of  $\text{Fe}^{2+/3+}-\text{C}\equiv\text{N}-\text{Ni}$ . The initial  
18  
19  
20  
21 charge and discharge capacities of NiHCF are 55 mAh/g and 60 mAh/g, respectively.  
22  
23

24 Although the capacity exhibited by NiHCF is lower when compared with gradient materials  
25  
26  
27 and MnHCF, NiHCF retains nearly 100% of its capacity after 100 cycles at 0.2 C (Figure  
28  
29  
30  
31 2b), displaying superior cycling stability. For the MnHCF cathode, two plateaus are  
32  
33  
34 observed (Figure 2a): the voltage plateau at 3.4V /3.2V for charge / discharge shows  
35  
36  
37 similar redox reactions as seen in NiHCF, and are attributed to the redox pair of  $\text{Fe}^{2+/3+}-$   
38  
39  
40  
41  $\text{C}\equiv\text{N}-\text{Mn}$ . In addition, a higher voltage plateau at 3.7V / 3.5 V (Figure S7) for charge /  
42  
43  
44 discharge is related to the redox reaction of  $\text{Fe}-\text{C}\equiv\text{N}-\text{Mn}^{2+/3+}$ . Figure S8 shows the  
45  
46  
47 charge/discharge (Figure S8a) and differential capacities versus voltage (dQ/dv) curves  
48  
49  
50  
51 (Figure S8b) of MnHCF cathodes during cycling. Structural reconstruction characteristics  
52  
53  
54  
55  
56  
57  
58  
59  
60

1  
2  
3 of loss of interstitial water from crystal structure causes the higher voltage plateau to  
4  
5  
6  
7 decrease by 0.2V over initial cycling.  
8  
9

10  
11 Owing to two active redox sites of  $\text{Fe}^{2+/3+}$  and  $\text{Mn}^{2+/3+}$  in  $\text{Fe-C}\equiv\text{N-Mn}$ , MnHCF exhibits  
12  
13  
14 the highest reversible capacity, however, its capacity retention is poor. As shown in Figure  
15  
16  
17  
18 2b, the discharge capacity of MnHCF decreases rapidly from 122 mAh/g to 64 mAh/g,  
19  
20  
21  
22 corresponding to a capacity retention of a meagre 52.5% after 100 cycles. The voltage  
23  
24  
25 plateaus become shorter and a larger overpotential is observed upon cycling. These  
26  
27  
28 inferior electrochemical properties of MnHCF in liquid electrolytes are consistent with  
29  
30  
31  
32 previous reports.<sup>29</sup>  
33  
34  
35  
36  
37  
38  
39  
40  
41  
42  
43  
44  
45  
46  
47  
48  
49  
50  
51  
52  
53  
54  
55  
56  
57  
58  
59  
60

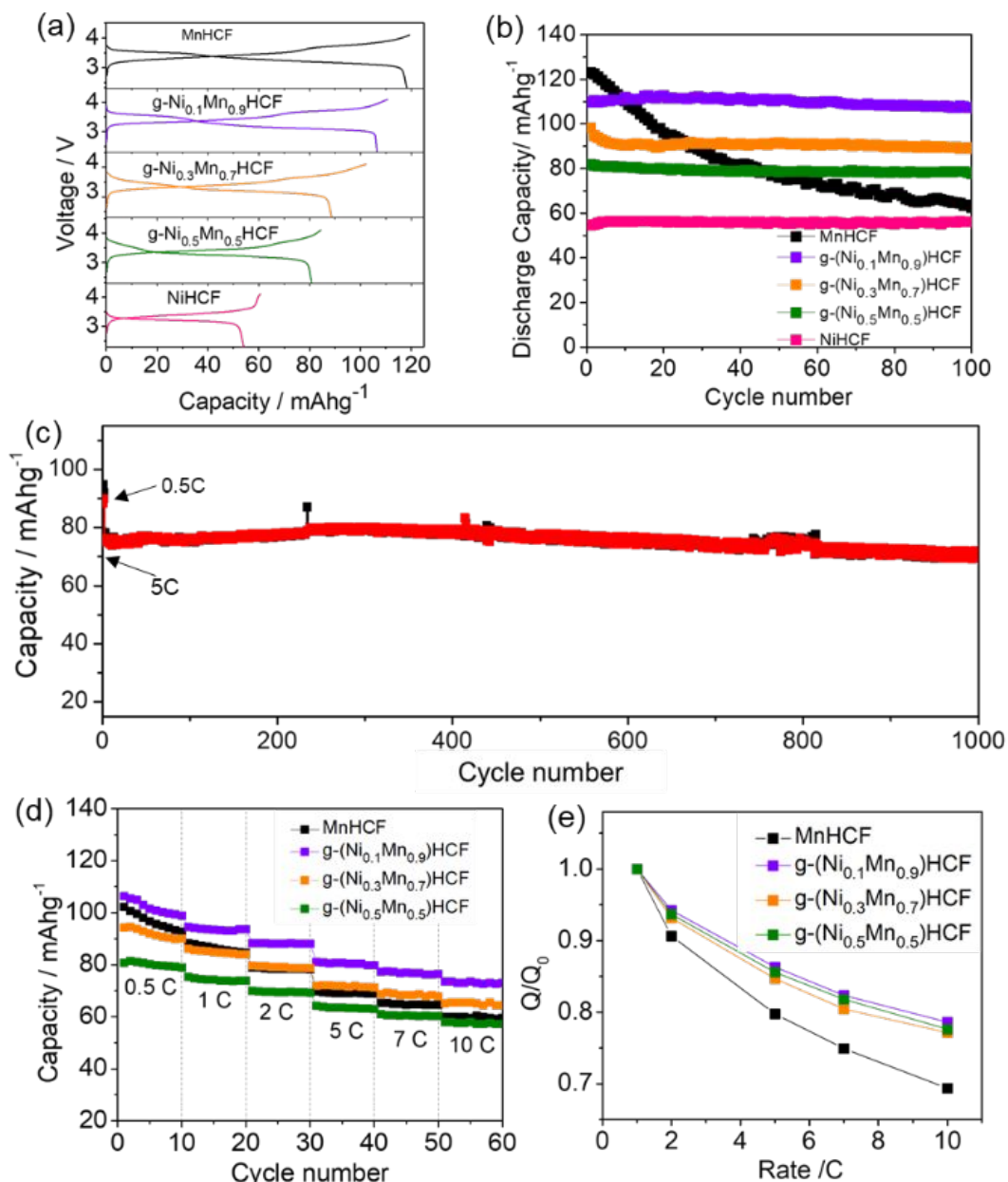


**Figure 2** (a) Charge/discharge curves and (b) cycling performance of gradient material, MnHCF and NiHCF at 0.2 C; (c) long-term cycling of the typical g-(Ni<sub>0.3</sub>Mn<sub>0.7</sub>)HCF at 5C; (d) rate capability and (e) normalized capacity of gradient materials at different C-rates.

1  
2  
3  
4 Different Ni:Mn ratios in the concentration-gradient cathodes, bring about changes in  
5  
6  
7 the reversible capacity and the voltage plateau. The voltage profiles (Figure 2a) of g-  
8  
9  
10  $(\text{Ni}_{0.5}\text{Mn}_{0.5})\text{HCF}$ , g- $(\text{Ni}_{0.3}\text{Mn}_{0.7})\text{HCF}$  and g- $(\text{Ni}_{0.1}\text{Mn}_{0.9})\text{HCF}$  reveal two plateaus at 3.4V  
11  
12 /3.2V and 3.7V / 3.5V when cycled between 2.0-4.1 V. The presence of the 3.2 V plateau  
13  
14 is indicative of the  $\text{Fe}^{2+/3+}$  redox couple which delivers a similar capacity to the  
15  
16  
17 homogenous MnHCF and NiHCF, whereas the high voltage plateau (3.5V/3.7V)  
18  
19  
20 associated with the redox couple of  $\text{Mn}^{2+/3+}$  becomes longer with the reduction of Ni in the  
21  
22  
23  
24  
25  
26  
27  
28  
29  
30  
31  
32  
33  
34  
35  
36  
37  
38  
39  
40  
41  
42  
43  
44  
45  
46  
47  
48  
49  
50  
51  
52  
53  
54  
55  
56  
57  
58  
59  
60  
particle. The reversible capacities (Figure 2b) of g- $(\text{Ni}_{0.1}\text{Mn}_{0.9})\text{HCF}$ , g- $(\text{Ni}_{0.3}\text{Mn}_{0.7})\text{HCF}$  and  
g- $(\text{Ni}_{0.5}\text{Mn}_{0.5})\text{HCF}$  are 110 mAh g<sup>-1</sup>, 98 mAh g<sup>-1</sup> and 82 mAh g<sup>-1</sup> at 0.2 C, respectively. It  
is seen that capacity decreased with the increasing Ni:Mn ratio and a lower Coulombic  
efficiency (C.E.) was seen in initial cycles, which might be attributed into the decomposition of  
electrolyte. The gradient-concentration materials showed a lower initial capacity than  
MnHCF, however, an improved cycling performance with a capacity retention of 95%,  
93% and 96% after 100 cycles was observed, which is considerably higher than that of  
MnHCF (52.5%). Such a trend was expected since NiFCH has a better stability, whereas  
MnHCF a higher capacity, however, the ability of just a small addition of Ni to increase

1  
2  
3 the stability so drastically was not anticipated. As shown in Figure S9, in comparison with  
4  
5  
6 the gradient materials, the non-gradient materials  $(\text{Ni}_{0.1}\text{Mn}_{0.9})\text{HCF}$  and  $(\text{Ni}_{0.3}\text{Mn}_{0.7})\text{HCF}$   
7  
8  
9 display capacity retentions of 86% and 84% after 100 cycles, respectively. The long-term cycling  
10  
11 stability was evaluated by galvanostatic charge/discharge tests at 0.5C for the first-two  
12  
13  
14 cycles and then at 5 C for 1000 cycles (Figure 2c). The g- $(\text{Ni}_{0.3}\text{Mn}_{0.7})\text{HCF}$  cathode  
15  
16  
17 delivered a high capacity retention of 93% after 1000 cycles (The capacity retention was  
18  
19  
20 calculated based on the value of 5C in Figure 2c). Comparing the XRD patterns for this  
21  
22  
23 cathode (Figure S10) from before and after cycling showed that no apparent changes  
24  
25  
26 occurred after 1000 cycles, in accordance with the stable long-term cycling performance  
27  
28  
29 of the gradient composite.  
30  
31  
32  
33  
34  
35  
36  
37  
38

39 The rate capability of the obtained materials was evaluated at different current  
40  
41 densities ranging from 0.5 C to 10 C in the voltage range of 2.0 ~ 4.1 V at room  
42  
43 temperature. As shown in Figure 2d, the capacity of the MnHCF cathode decreased  
44  
45  
46 rapidly with increasing the current density from 100 mAh/g at 1 C to 60 mAh/g at 10 C. In  
47  
48  
49 contrast, the g-NiMnHCF samples maintained most of their capacity and showed  
50  
51  
52  
53  
54  
55  
56  
57  
58  
59  
60

1  
2  
3  
4 excellent rate capabilities in a wide range of current densities. The separation of the  
5  
6  
7 potential (Figure S11) between charge and discharge increased slightly with increasing  
8  
9  
10 the C-rate, implying the weak polarization and overpotential during the electrochemical  
11  
12  
13 process. A discharge capacity of 110 mAh g<sup>-1</sup> and 100 mAh g<sup>-1</sup> was observed for the g-  
14  
15  
16 (Ni<sub>0.1</sub>Mn<sub>0.9</sub>)HCF cathode at 0.5 C and 1 C, respectively, and decreased slightly with  
17  
18  
19 increasing the C-rate. The electrode exhibited a high capacity of 72 mAh g<sup>-1</sup> at 10 C,  
20  
21  
22 corresponding to a 78% capacity retention at 1 C. Although the g-(Ni<sub>0.5</sub>Mn<sub>0.5</sub>)HCF cathode  
23  
24  
25 delivered the lowest specific capacity at 0.5 C due to the inactivity of Ni<sup>2+</sup>, it exhibited the  
26  
27  
28 least capacity decay with an increase in current density, indicating the excellent high-rate  
29  
30  
31  
32  
33  
34  
35  
36  
37  
38  
39  
40  
41  
42  
43  
44  
45  
46  
47  
48  
49  
50  
51  
52  
53  
54  
55  
56  
57  
58  
59  
60  
least capacity decay with an increase in current density, indicating the excellent high-rate  
capability.

Figure 2e compares the normalized capacity ( $Q/Q_0$ ) of the samples at different current densities.  $Q$  is the capacity at different C-rates, and  $Q_0$  is the capacity of electrodes at 1 C. The normalized capacity of g-NiMnHCF was higher than that of the MnHCF cathode at current densities ranging from 2 C to 10 C. The g-(Ni<sub>0.5</sub>Mn<sub>0.5</sub>)HCF cathode retained 78% of its capacity when cycled at 10 C against just the 67% retention

1  
2  
3 MnHCF. This further supports the excellent electrochemical performance of gradient  
4  
5  
6  
7 materials (g-(Ni<sub>0.1</sub>Mn<sub>0.9</sub>)HCF, g-(Ni<sub>0.3</sub>Mn<sub>0.7</sub>)HCF and g-(Ni<sub>0.5</sub>Mn<sub>0.5</sub>)HCF) in terms of cycling  
8  
9  
10 stability and rate capability achieved, with minimal sacrifice of the specific capacity when  
11  
12  
13 compared with homogenous MnHCF. The high rate capability is determined by a fast ion  
14  
15  
16 diffusion and charge transfer in the electrode during the electrochemical process. The  
17  
18  
19 diffusion coefficient of Na<sup>+</sup> ( $D_{\text{Na}^+}$ ) in the cathode (g-(Ni<sub>0.1</sub>Mn<sub>0.9</sub>)HCF and MnHCF) was  
20  
21  
22 estimated from cyclic voltammograms (CV) with varying scan speeds by the Randles–  
23  
24  
25 Sevcik method.<sup>33-34</sup> As shown in Figure S12, the  $D_{\text{Na}^+}$  value in the g-(Ni<sub>0.1</sub>Mn<sub>0.9</sub>)HCF  
26  
27  
28 cathode during sodiation and desodiation was  $4.8 \times 10^{-11} \text{ cm}^2 \text{ s}^{-1}$  and  $5.9 \times 10^{-11} \text{ cm}^2 \text{ s}^{-1}$ ,  
29  
30  
31  
32 respectively, which is higher than  $D_{\text{Na}^+}$  in the pure MnHCF cathode ( $2.4 \times 10^{-11} \text{ cm}^2 \text{ s}^{-1}$  for  
33  
34  
35 sodiation and  $3.8 \times 10^{-11} \text{ cm}^2 \text{ s}^{-1}$  for desodiation). Therefore, the gradient substitution by Ni  
36  
37  
38 enhanced the Na<sup>+</sup> diffusivity in the electrode, resulting into the faster rate capability.  
39  
40  
41  
42  
43  
44  
45  
46  
47  
48  
49  
50  
51  
52  
53  
54  
55  
56  
57  
58  
59  
60

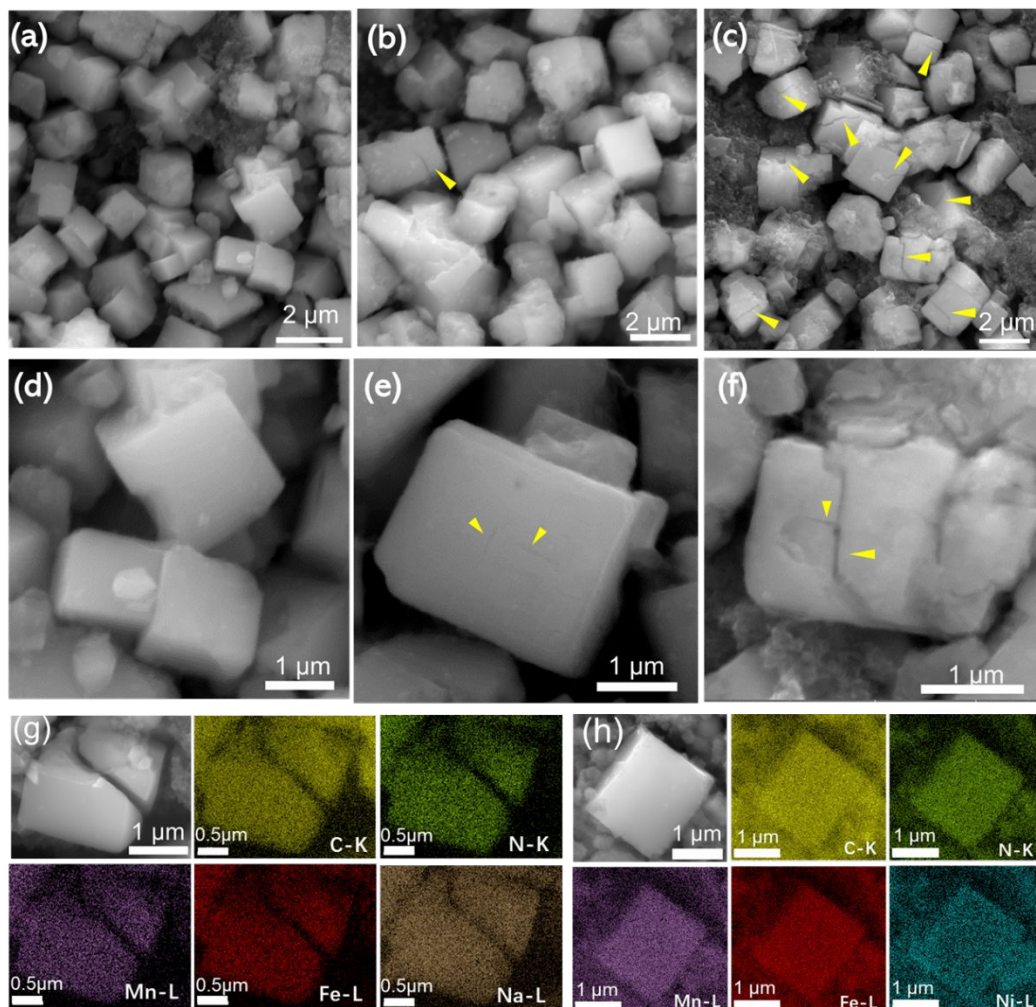


**Figure 3** (a-c) Low magnification SEM images of MnHCF materials after (a) 10, (b) 20 and (c) 50 cycles. (d-f) High magnification SEM images of MnHCF materials after (d) 10, (e) 20 and (f) 50 cycles. (g-h) SEM images and element mapping of (g) MnHCF and (h) g-(Ni<sub>0.1</sub>Mn<sub>0.9</sub>)HCF after 100 cycles.

1  
2  
3  
4 Scanning electron microscopy (SEM) was performed to determine the initiation and  
5  
6  
7 propagation of fracture in the PBA cathodes upon cycling. Figure S13 shows the  
8  
9  
10 morphology of active particles for the MnHCF (Figure S13a) and g-(Ni<sub>0.1</sub>Mn<sub>0.9</sub>)HCF  
11  
12  
13 (Figure S13b) cathodes before cycling. As shown in **Figure 3**, the MnHCF particles  
14  
15  
16 retained their cubic shape and size upon cycling, however, the morphology of their  
17  
18  
19 surface changed and became rougher/coarser. Such morphological changes can be  
20  
21  
22 attributed into the dissolution of Mn<sup>2+</sup> into the organic electrolyte,<sup>29</sup> leading to corrosion of  
23  
24  
25 the surface. MnHCF active particles exhibited no obvious signs of fracture after 10 cycles,  
26  
27  
28 however small-scale crack initiation and propagation was observed from 20 cycles  
29  
30  
31 (Figure 3b and e). After 50 cycles (Figure 3c), fracture was observed in almost every  
32  
33  
34 particle. The cracks appeared on the face center of each particle. The crack width after  
35  
36  
37 100 cycles (Figure 3g) was measured to be ~ 100 nm. These experimental observations  
38  
39  
40 can interpret the capacity decay that is seen in Figure 2b after 100 cycles. It is expected  
41  
42  
43 that the structural changes in the form of phase transitions and/or volume expansions  
44  
45  
46 during sodiation can induce strain/stress in the active particles, resulting in mechanical  
47  
48  
49 damage and capacity fade. Moreover, comparing the XRD patterns at different states of  
50  
51  
52  
53  
54  
55  
56  
57  
58  
59  
60

1  
2  
3 charge (Figure S14a) showed that splitting peaks at  $\sim 23.7^\circ$  and  $37.9^\circ$  in the pristine  
4  
5  
6  
7 electrode are merged into sharp single peaks at the charged state, due to the phase  
8  
9  
10 transformation from monoclinic to cubic. The peaks of the charged electrode shifted to a  
11  
12  
13 slightly lower angle, suggesting the expansion of the lattice during the  $\text{Na}^+$  extraction  
14  
15  
16  
17 process. All diffraction peaks returned to their pristine state after complete sodiation,  
18  
19  
20  
21 illustrating that the phase transformation was reversible during charge/discharge,  
22  
23  
24 however, the electrode suffered a  $\sim 8.5\%$  volume change during this process (as  
25  
26  
27  
28 determined by refining the XRD peaking with the Fullprof software), which is consistent  
29  
30  
31 with previous studies.<sup>26</sup> These structural changes would contribute to the fracture of the  
32  
33  
34 active particles. Such fracture disrupts the electronic conductivity and ionic diffusion in  
35  
36  
37  
38 the electrode, moreover corrosion causes parasitic side reactions on the newly formed  
39  
40  
41  
42 surfaces, thus leading to a continuous capacity fade. In contrast, the gradient material g-  
43  
44  
45  $(\text{Ni}_{0.1}\text{Mn}_{0.9})\text{HCF}$  cathode retained its structural integrity during cycling, as no obvious  
46  
47  
48  
49 cracking was observed after 100 cycles (Figure 3h).  
50  
51  
52  
53  
54  
55  
56  
57  
58  
59  
60

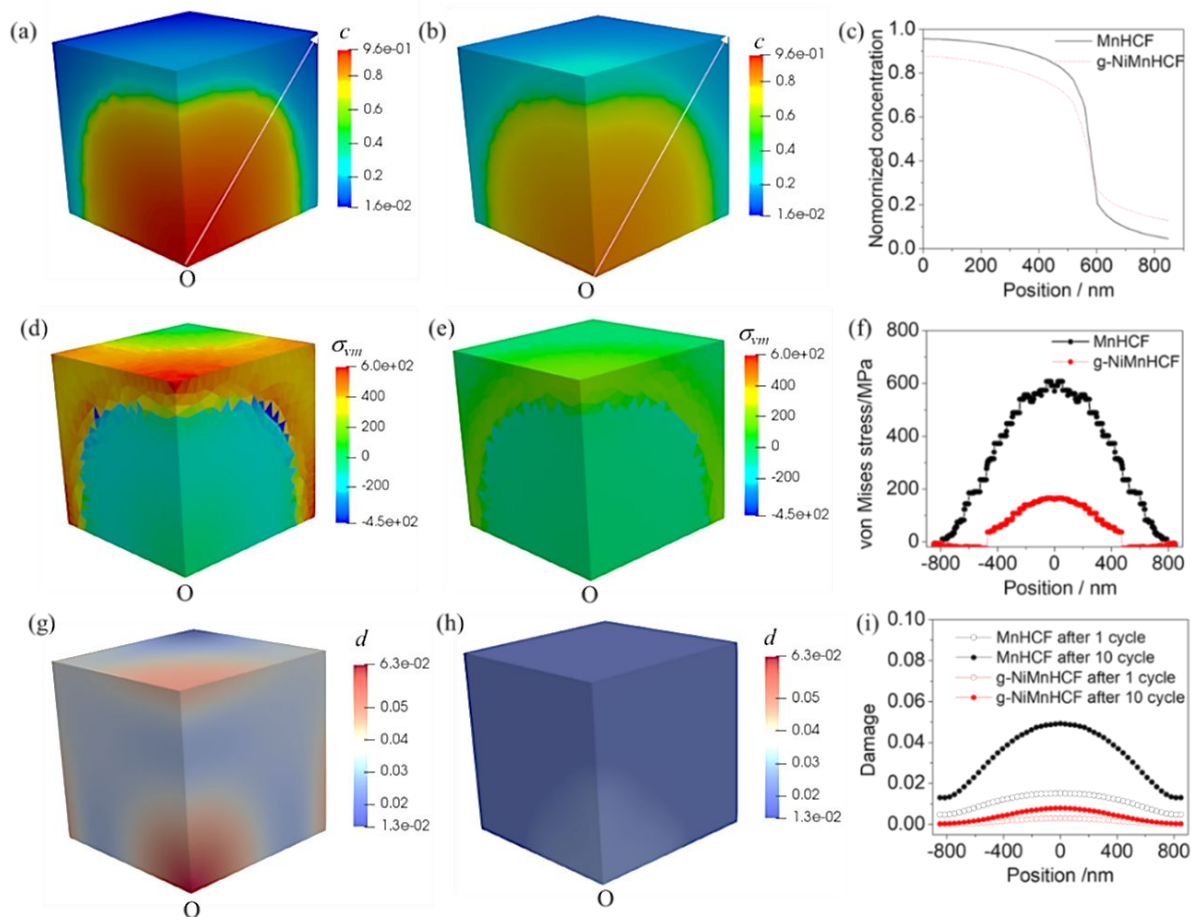


**Figure 4.** Chemomechanical simulation results showing damage evolution and stress generation in MnHCF and g-NiMnHCF during electrochemical cycling. (a)-(b) Concentration distribution in one-eighth unit cell at 50% state of charge (SOC) for (a) MnHCF and (b) g-NiMnHCF. (c) Concentration profiles from the center of the particle to the edge center of the top surface (along white arrows in a and b). (d)-(f) Modulated von Mises stress ( $\sigma_{vm}$ ) distribution in MnHCF (d) and g-NiMnHCF (e) during cycling. (f) von Mises stress profiles. (g)-(h) Damage distribution in MnHCF (g) and g-NiMnHCF (h) after cycling. (i) Damage profiles after 1 and 10 cycles for MnHCF and g-NiMnHCF.

1  
2  
3  
4 Comparison of modulated von Mises stress profiles along the diagonal line on the top  
5  
6  
7 surface of MnHCF and g-NiMnHCF. (g)-(h) Damage distribution of MnHCF (g) and g-  
8  
9  
10 NiMnHCF (h) materials after 10 cycles respectively. (i) Comparison of damage profiles  
11  
12  
13 along the diagonal line on the top surface of MnHCF and g-NiMnHCF after 10 cycles.  
14  
15  
16  
17

18 To gain a thorough understanding of crack formation, finite element simulations  
19  
20  
21 were performed to model diffusion-induced stresses and damage in active particles  
22  
23  
24 during repeated electrochemical cycles using the model presented in Ref [35]. Considering  
25  
26  
27 symmetry, only one-eighth of the cubic particle was modelled. As shown in Figure S17a,  
28  
29  
30 the letter "O" marks the center of the particle. Two different compositions MnHCF and g-  
31  
32  
33 NiMnHCF were considered. Since both materials undergo a two-phase reaction  
34  
35  
36 mechanism (monoclinic to cubic phase transition) during sodiation/desodiation, at each  
37  
38  
39 intermediate state the active particle was treated as a core-shell-like cubic structure,  
40  
41  
42 where the core region was the pristine part and the shell region was the de-sodiated  
43  
44  
45 region. Contour plots (**Figure 4a** and b) of the normalized Na<sup>+</sup> concentration ( $C_{\text{Na}^+}$ )  
46  
47  
48 obtained by the concentration-dependent diffusivity equation (as shown in Eq-S1) show  
49  
50  
51  
52  
53  
54  
55  
56  
57  
58  
59  
60

1  
2  
3 a sharp phase reaction and steep distribution of  $C_{\text{Na}^+}$ , which would cause an abrupt  
4  
5  
6  
7 change of stresses in the two-phase regions; where the core region is under compressive  
8  
9  
10 (negative) stress while the shell is under tensile (positive) stress during desodiation (as  
11  
12  
13 shown Figure 4d and e). Therefore, there is a jump of the hydrostatic stress ( $\sigma_h = \text{tr}(\sigma)/3$ )  
14  
15  
16 at the de-sodiation reaction front. Figure 4c compares the diagonal distributions of  $C_{\text{Na}^+}$   
17  
18  
19 in MnHCF and g- NiMnHCF. The profile for  $C_{\text{Na}^+}$  is less steep for g-NiMnHCF than for  
20  
21  
22 MnHCF due to the faster diffusion of  $\text{Na}^+$  in g-NiMnHCF. It should also be noted that g-  
23  
24  
25 MnHCF has a much lower volume expansion (0.29%) than that of MnHCF (8.5%). Both  
26  
27  
28 NiMnHCF has a much lower volume expansion (0.29%) than that of MnHCF (8.5%). Both  
29  
30  
31 factors lead to a significantly lower Von Mises stress than in MnHCF.  
32  
33  
34

35  
36 The von Mises stress ( $\sigma_v$ ) distribution was investigated since it's the main factor  
37  
38  
39 contributing to plastic deformation and fracture. Figure 4(d-e) depicts the contour plots of  
40  
41  
42 the modulated von Mises stress ( $\sigma_{vm} = \text{sign}(\sigma_h) \times \sigma_v$  where  $\text{sign}(\sigma_h)$  represents the sign  
43  
44  
45 function of  $\sigma_h$  and its value is 1 when  $\sigma_h > 0$  and -1 when  $\sigma_h < 0$ ) for MnHCF and g-NiMnHCF  
46  
47  
48 at a 50% state of charge (SOC). The maximum value for  $\sigma_v$  is located near the  
49  
50  
51 core(pristine)-shell(sodiated) interface. Figure 4f compares the  $\sigma_{vm}$  distributions along the  
52  
53  
54  
55  
56  
57  
58  
59  
60

1  
2  
3 diagonal direction on the surfaces of the particle. The maximum  $\sigma_v$  is also observed at  
4  
5  
6  
7 the center of the cubic particles, however, there is an appreciable difference in the  
8  
9  
10 magnitude of the observed stress in MnHCF (607 MPa) and g-NiMnHCF (165 MPa). The  
11  
12  
13 maximum  $\sigma_v$  in MnHCF is nearly 4 times of that in g-NiMnHCF. It should also be noted  
14  
15  
16 that for g-NiMnHCF, the region under tension is of very limited volume contrary to what  
17  
18  
19 occurs in MnHCF (Figure 4f). Almost the entire external surface of MnHCF is under  
20  
21  
22 tension whereas in g-NiMnHCF only the region near the vertex is in compression.  
23  
24  
25  
26  
27  
28

29 The damage evolution is further simulated to understand the impact of different  
30  
31 compositions on the mechanical degradation of the particles. Since no pre-existing cracks  
32  
33 or flaws were considered in the simulation, the damage profiles are similar during initial  
34  
35  
36 cycling, for both homogeneous and gradient cathodes, as shown in Figure S18 and Figure  
37  
38  
39 4g-h, which demonstrate the damage profiles of MnHCF and g-NiMnHCF after the 1<sup>st</sup> and  
40  
41  
42 10<sup>th</sup> cycle, respectively. A scalar phase-field variable  $d$  ranging from 0 to 1 ( $d=0$  for  
43  
44  
45 unbroken/intact state, and  $d=1$  for fully broken damaged state) is defined. Damage in  
46  
47  
48  
49  
50  
51  
52  
53 MnHCF was localized near the center of the external surfaces as well as near the center  
54  
55  
56  
57  
58  
59  
60

1  
2  
3 of the particles, while damage in g-NiMnHCF particles, was confined to the center of the  
4  
5  
6  
7 cell (Figure 4h). Figure S18 shows that the maximum damage increased upon cycling for  
8  
9  
10 both MnHCF and g-NiMnHCF, however, the damage values at the particle center and  
11  
12  
13 surface center of MnHCF increased to 6.35% and 4.83% after 10 cycles, which is much  
14  
15  
16  
17 higher when compared with g-NiMnHCF (1.96% and 0.79%, respectively). g-NiMnHCF  
18  
19  
20 exhibited alleviation of accumulated damage in the vicinity of the face center. Figure 4i  
21  
22  
23 shows the damage distribution of MnHCF and g-NiMnHCF along the diagonal line on the  
24  
25  
26  
27 top surface after 1 and 10 cycles, respectively. Similar damage profiles were observed,  
28  
29  
30  
31 however, the magnitudes were significantly different; the maximum damage values for  
32  
33  
34 MnHCF being 1.52% and 4.92% and for g-NiMnHCF being 0.31% and 0.80% after 1 and  
35  
36  
37  
38 10 cycles, respectively. Both homogenous and concentration-gradient particles  
39  
40  
41 demonstrate about a 3-fold increase in maximum damage over the 1<sup>st</sup> and 10<sup>th</sup> cycle,  
42  
43  
44  
45 even though for the g-NiMnHCF it is negligible. Fracture is likely to occur in regions  
46  
47  
48 showing increased damage upon cycling, and therefore if the simulation for the  
49  
50  
51 homogeneous materials was run over 20 cycles, cracks would nucleate as in the  
52  
53  
54  
55 experimental images. However, due to computational costs simulations were stopped  
56  
57  
58  
59  
60

after 10 cycles. In Figure 4 it is seen that the predicted damage value is significantly low in g-NiMnHCF particles, and no cracks were anticipated. Therefore, g-NiMnHCF has a much better mechanical performance than MnHCF.

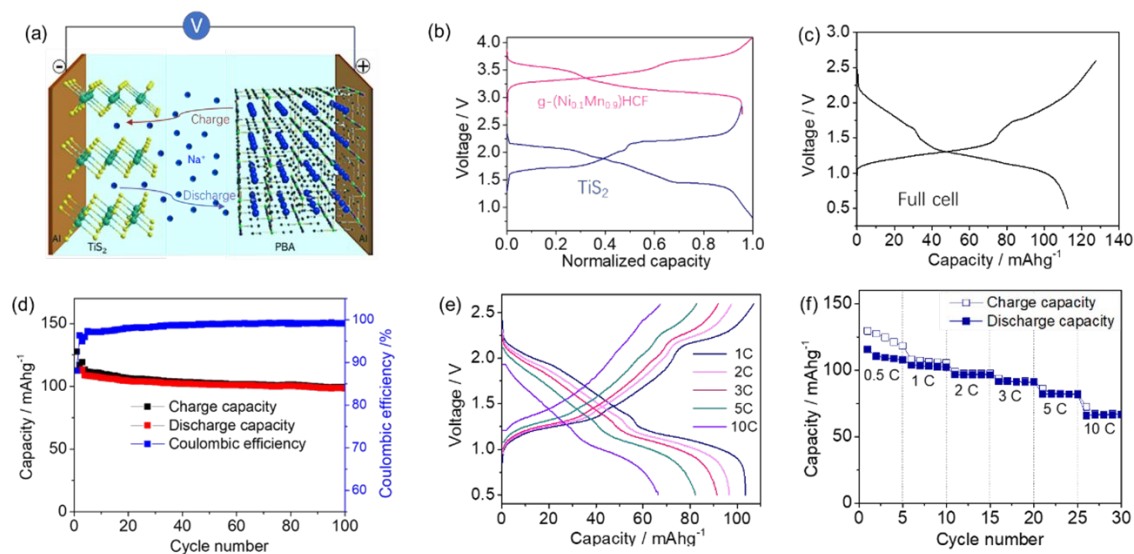


**Figure 5** (a) Schematic mechanism of full cell that using g-NiMnHCF as cathode and TiS<sub>2</sub> as anode. (b) Charge/discharge profiles of g-Ni<sub>0.1</sub>Mn<sub>0.9</sub>HCF and TiS<sub>2</sub> in half cell. (c) The first charge/discharge curves of the full cell using g-Ni<sub>0.1</sub>Mn<sub>0.9</sub>HCF as cathode and TiS<sub>2</sub> as anode. (d) Cycling performance of the full cell at 0.5 C. (e) Charge/discharge curve and rate capability of the full cell at different C-rate. (f) The capacity was calculated by the cathode mass.

1  
2  
3 Sodium metal is not an ideal anode for commercial batteries due to its high reactivity  
4  
5  
6 with the electrolyte and dendrite formation<sup>36</sup>, which results in safety issues. Carbon-based  
7  
8  
9 materials such as hard carbon and graphite are commonly used as anodes for Na-ion full  
10  
11  
12 cells. However, the potential plateau of hard carbon is close to the plating potential of Na,  
13  
14  
15 leading to the formation of Na dendrites during the charge process.<sup>37-38</sup> In testing the  
16  
17  
18 present gradient PBAs in a full cell, graphitic anodes were considered first, which cycle  
19  
20  
21 only in glyme electrolyte. In Figure S15a and b it is seen that a capacity of 125 mAh g<sup>-1</sup>  
22  
23  
24 and a low initial Coulombic efficiency (C.E.) of 70% were obtained after the first cycle. In  
25  
26  
27  
28  
29  
30  
31 Figure S15c it is seen that although the g-(Ni<sub>0.1</sub>Mn<sub>0.9</sub>)HCF/graphite full cell displayed a  
32  
33  
34 stable discharge capacity within 100 cycles, it delivered a low C.E. of 50%. Therefore,  
35  
36  
37  
38  
39  
40  
41  
42  
43  
44  
45  
46  
47  
48  
49  
50  
51  
52  
53  
54  
55  
56  
57  
58  
59  
60

activation of the graphite anode is required before coupling with the cathode to assemble  
a full cell. Our previous research demonstrated that TiS<sub>2</sub>/Na half-cells presented superior  
electrochemical performance in carbonate-based electrolyte. Herein, therefore a layered-  
type TiS<sub>2</sub> with particle size of ~ 5 μm (Figure S16b) was chosen as the anode. The strong  
(001) diffraction peak (Figure S16a) implied a highly preferred orientation along the *c*-axis  
direction and good S-Ti-S layer stacks. Using TiS<sub>2</sub> in a half Na-ion cell allowed to obtain

1  
2  
3 a high reversible capacity of 200 mAh g<sup>-1</sup> at 0.5C, initial Coulombic efficiency (95%),  
4  
5  
6  
7 cycling stability and rate capability (157 mAh g<sup>-1</sup> at 5 C, 122 mAh g<sup>-1</sup> at 10 C ), as seen in  
8  
9  
10 Figure S16c-d.

11  
12  
13  
14 A full cell, as illustrated in **Figure 5a**, was therefore assembled by using g-  
15  
16 (Ni<sub>0.1</sub>Mn<sub>0.9</sub>)HCF as the cathode, TiS<sub>2</sub> as the anode and 1 M NaPF<sub>6</sub> in EC/DMC with 5%  
17  
18  
19  
20  
21  
22  
23  
24  
25  
26  
27  
28  
29  
30  
31  
32  
33  
34  
35  
36  
37  
38  
39  
40  
41  
42  
43  
44  
45  
46  
47  
48  
49  
50  
51  
52  
53  
54  
55  
56  
57  
58  
59  
60  
61  
62  
63  
64  
65  
66  
67  
68  
69  
70  
71  
72  
73  
74  
75  
76  
77  
78  
79  
80  
81  
82  
83  
84  
85  
86  
87  
88  
89  
90  
91  
92  
93  
94  
95  
96  
97  
98  
99  
100  
101  
102  
103  
104  
105  
106  
107  
108  
109  
110  
111  
112  
113  
114  
115  
116  
117  
118  
119  
120  
121  
122  
123  
124  
125  
126  
127  
128  
129  
130  
131  
132  
133  
134  
135  
136  
137  
138  
139  
140  
141  
142  
143  
144  
145  
146  
147  
148  
149  
150  
151  
152  
153  
154  
155  
156  
157  
158  
159  
160  
161  
162  
163  
164  
165  
166  
167  
168  
169  
170  
171  
172  
173  
174  
175  
176  
177  
178  
179  
180  
181  
182  
183  
184  
185  
186  
187  
188  
189  
190  
191  
192  
193  
194  
195  
196  
197  
198  
199  
200  
201  
202  
203  
204  
205  
206  
207  
208  
209  
210  
211  
212  
213  
214  
215  
216  
217  
218  
219  
220  
221  
222  
223  
224  
225  
226  
227  
228  
229  
230  
231  
232  
233  
234  
235  
236  
237  
238  
239  
240  
241  
242  
243  
244  
245  
246  
247  
248  
249  
250  
251  
252  
253  
254  
255  
256  
257  
258  
259  
260  
261  
262  
263  
264  
265  
266  
267  
268  
269  
270  
271  
272  
273  
274  
275  
276  
277  
278  
279  
280  
281  
282  
283  
284  
285  
286  
287  
288  
289  
290  
291  
292  
293  
294  
295  
296  
297  
298  
299  
300  
301  
302  
303  
304  
305  
306  
307  
308  
309  
310  
311  
312  
313  
314  
315  
316  
317  
318  
319  
320  
321  
322  
323  
324  
325  
326  
327  
328  
329  
330  
331  
332  
333  
334  
335  
336  
337  
338  
339  
340  
341  
342  
343  
344  
345  
346  
347  
348  
349  
350  
351  
352  
353  
354  
355  
356  
357  
358  
359  
360  
361  
362  
363  
364  
365  
366  
367  
368  
369  
370  
371  
372  
373  
374  
375  
376  
377  
378  
379  
380  
381  
382  
383  
384  
385  
386  
387  
388  
389  
390  
391  
392  
393  
394  
395  
396  
397  
398  
399  
400  
401  
402  
403  
404  
405  
406  
407  
408  
409  
410  
411  
412  
413  
414  
415  
416  
417  
418  
419  
420  
421  
422  
423  
424  
425  
426  
427  
428  
429  
430  
431  
432  
433  
434  
435  
436  
437  
438  
439  
440  
441  
442  
443  
444  
445  
446  
447  
448  
449  
450  
451  
452  
453  
454  
455  
456  
457  
458  
459  
460  
461  
462  
463  
464  
465  
466  
467  
468  
469  
470  
471  
472  
473  
474  
475  
476  
477  
478  
479  
480  
481  
482  
483  
484  
485  
486  
487  
488  
489  
490  
491  
492  
493  
494  
495  
496  
497  
498  
499  
500  
501  
502  
503  
504  
505  
506  
507  
508  
509  
510  
511  
512  
513  
514  
515  
516  
517  
518  
519  
520  
521  
522  
523  
524  
525  
526  
527  
528  
529  
530  
531  
532  
533  
534  
535  
536  
537  
538  
539  
540  
541  
542  
543  
544  
545  
546  
547  
548  
549  
550  
551  
552  
553  
554  
555  
556  
557  
558  
559  
560  
561  
562  
563  
564  
565  
566  
567  
568  
569  
570  
571  
572  
573  
574  
575  
576  
577  
578  
579  
580  
581  
582  
583  
584  
585  
586  
587  
588  
589  
590  
591  
592  
593  
594  
595  
596  
597  
598  
599  
600  
601  
602  
603  
604  
605  
606  
607  
608  
609  
610  
611  
612  
613  
614  
615  
616  
617  
618  
619  
620  
621  
622  
623  
624  
625  
626  
627  
628  
629  
630  
631  
632  
633  
634  
635  
636  
637  
638  
639  
640  
641  
642  
643  
644  
645  
646  
647  
648  
649  
650  
651  
652  
653  
654  
655  
656  
657  
658  
659  
660  
661  
662  
663  
664  
665  
666  
667  
668  
669  
670  
671  
672  
673  
674  
675  
676  
677  
678  
679  
680  
681  
682  
683  
684  
685  
686  
687  
688  
689  
690  
691  
692  
693  
694  
695  
696  
697  
698  
699  
700  
701  
702  
703  
704  
705  
706  
707  
708  
709  
710  
711  
712  
713  
714  
715  
716  
717  
718  
719  
720  
721  
722  
723  
724  
725  
726  
727  
728  
729  
730  
731  
732  
733  
734  
735  
736  
737  
738  
739  
740  
741  
742  
743  
744  
745  
746  
747  
748  
749  
750  
751  
752  
753  
754  
755  
756  
757  
758  
759  
760  
761  
762  
763  
764  
765  
766  
767  
768  
769  
770  
771  
772  
773  
774  
775  
776  
777  
778  
779  
780  
781  
782  
783  
784  
785  
786  
787  
788  
789  
790  
791  
792  
793  
794  
795  
796  
797  
798  
799  
800  
801  
802  
803  
804  
805  
806  
807  
808  
809  
810  
811  
812  
813  
814  
815  
816  
817  
818  
819  
820  
821  
822  
823  
824  
825  
826  
827  
828  
829  
830  
831  
832  
833  
834  
835  
836  
837  
838  
839  
840  
841  
842  
843  
844  
845  
846  
847  
848  
849  
850  
851  
852  
853  
854  
855  
856  
857  
858  
859  
860  
861  
862  
863  
864  
865  
866  
867  
868  
869  
870  
871  
872  
873  
874  
875  
876  
877  
878  
879  
880  
881  
882  
883  
884  
885  
886  
887  
888  
889  
890  
891  
892  
893  
894  
895  
896  
897  
898  
899  
900  
901  
902  
903  
904  
905  
906  
907  
908  
909  
910  
911  
912  
913  
914  
915  
916  
917  
918  
919  
920  
921  
922  
923  
924  
925  
926  
927  
928  
929  
930  
931  
932  
933  
934  
935  
936  
937  
938  
939  
940  
941  
942  
943  
944  
945  
946  
947  
948  
949  
950  
951  
952  
953  
954  
955  
956  
957  
958  
959  
960  
961  
962  
963  
964  
965  
966  
967  
968  
969  
970  
971  
972  
973  
974  
975  
976  
977  
978  
979  
980  
981  
982  
983  
984  
985  
986  
987  
988  
989  
990  
991  
992  
993  
994  
995  
996  
997  
998  
999  
1000

A full cell, as illustrated in **Figure 5a**, was therefore assembled by using g-(Ni<sub>0.1</sub>Mn<sub>0.9</sub>)HCF as the cathode, TiS<sub>2</sub> as the anode and 1 M NaPF<sub>6</sub> in EC/DMC with 5% FEC as the electrolyte. Figure 5b shows charge/discharge profiles of voltage vs. normalized capacity for g-(Ni<sub>0.1</sub>Mn<sub>0.9</sub>)HCF and TiS<sub>2</sub> electrodes. The voltage difference between the two electrodes determines the working voltage of the full cell. As shown in Figure 5c, the full cell presents two potential profiles at ~1.2 V and ~2.1V. The initial charge and discharge capacities were 127 mA h g<sup>-1</sup> and 112 mA h g<sup>-1</sup> at 0.5 C in the potential range of 0.5-2.6V, exhibiting a high initial C.E. of 88.1%. High C.E. benefits from the highly reversible nature of both the cathode and anode materials. The cycling stability of the full cell was examined at 1C. As shown in Figure 5d, the reversible capacity of the cathode in the full cell reached 110 mA h g<sup>-1</sup> and a capacity retention of 87.5% was observed over 100 cycles. Figure 5(e-f) shows that the capacity decreased slightly as the

1  
2  
3 rate increased from 0.5 C to 10 C. At 5 C and 10 C, it still achieved a capacity of 88 mAh  
4  
5  
6  
7  $\text{g}^{-1}$  and 70 mAh  $\text{g}^{-1}$ , implying excellent rate capability. Comparing with the performance of  
8  
9  
10 full cells reported in previous studies (Table S3), our results show a superior rate  
11  
12  
13 capability, initial C.E and stability, which indicates a great advance over the state-of-the-  
14  
15  
16 art of sodium-ion batteries. The output voltage of the full cell is lower than the organic cell  
17  
18 using carbon and alloying anode, but it is in the stable potential window of the aqueous  
19  
20  
21 electrolyte, making it feasible to run in an aqueous electrolyte. The aqueous SIBs based  
22  
23  
24 on these materials will be studied in-depth in further work.  
25  
26  
27  
28  
29  
30  
31

32 In conclusion, concentration-gradient materials g-NiMnHCF were successfully  
33  
34 synthesized via a facile co-precipitation process, resulting in a Ni rich shell and Mn core.  
35  
36  
37 The expansion of NiHCF upon sodiation is less than 1%, whereas that of MnHCF is 8.5%,  
38  
39  
40 hence this gradient microstructure allows to buffer the core volume changes. The as-  
41  
42  
43 obtained gradient microstructure cathodes exhibited outstanding cycling stability and rate  
44  
45  
46 capability, when compared with the homogenous MnHCF cathodes. SEM images  
47  
48  
49 revealed that after twenty cycles cracks initiated and propagated at the center of the  
50  
51  
52  
53  
54  
55  
56  
57  
58  
59  
60

1  
2  
3 MnHCF particles, but no damage occurred in the g-NiMnHCF. The superior  
4  
5  
6  
7 electrochemical performance of g-NiMnHCF could therefore be attributed to its stable  
8  
9  
10 structure and fast ionic diffusivity, which reduce the mechanical degradation induced by  
11  
12  
13 diffusion at the reaction front during charge/discharge. The experimental data were  
14  
15  
16 interpreted with phase field modeling which showed that g-NiMnHCF experiences lower  
17  
18  
19 von Mises stresses and hydrostatic stress levels and negligible damage, while MnHCF  
20  
21  
22 with a uniform composition undergoes higher stresses, and the damage tends to localize  
23  
24  
25 at regions close to the particle center and face centers. The maximum damage for MnHCF  
26  
27  
28 is more than 3 times as that for g-NiMnHCF. As a result, g-NiMnHCF shows better  
29  
30  
31 damage tolerance and its mechanical degradation due to excessive stresses can be  
32  
33  
34 effectively retarded. In concluding, a full cell using  $\text{TiS}_2$  as the anode and g-NiMnHCF as  
35  
36  
37 the cathode was shown to have an outstanding initial Coulombic efficiency, capacity  
38  
39  
40 retention and rate capability, demonstrating potential practical applications in energy  
41  
42  
43 storage. Therefore, designing gradient composition materials is an effective approach to  
44  
45  
46 improve the stability of PBA cathodes. We also believe that this approach can be  
47  
48  
49  
50  
51  
52  
53  
54  
55  
56  
57  
58  
59  
60

1  
2  
3 reasonably extended to other electrode materials to solve the mechanical degradation in  
4  
5  
6  
7 LIBs and SIBs.  
8  
9

## 10 11 **Supporting Information.** 12

13  
14  
15  
16 The Supporting Information is available free of charge on the ACS Publications website  
17  
18  
19 at DOI:xxxx.  
20  
21  
22

23  
24 Experimental details of preparation, characterizations and simulations. Additional  
25  
26  
27 figures and tables showing TGA, XRD, ICP, SEM, and simulation results.  
28  
29  
30

## 31 32 **Notes** 33

34  
35  
36 The authors declare no competing financial interest.  
37  
38  
39

## 40 41 **Acknowledgements** 42

43  
44  
45 The authors are grateful to the National Science Foundation for supporting this work  
46  
47  
48 through the CMMI grant (CMMI-1762602).  
49  
50

## 51 52 **References** 53 54 55 56 57 58 59 60

- 1  
2  
3  
4 1. Goodenough, J. B.; Park, K.-S., The Li-Ion Rechargeable Battery: A Perspective.  
5  
6  
7 *J. Am. Chem. Soc.* **2013**, *135*, 1167-1176.  
8  
9
- 10  
11 2. Scrosati, B.; Hassoun, J.; Sun, Y. K., Lithium-ion batteries. A look into the future.  
12  
13  
14 *Energy Environ. Sci.* **2011**, *4*, 3287-3295.  
15  
16
- 17  
18 3. Zuo, Y. X.; Li, B. A.; Jiang, N.; Chu, W. S.; Zhang, H.; Zou, R. Q.; Xia, D. G., A  
19  
20 High-Capacity O2-Type Li-Rich Cathode Material with a Single-Layer Li<sub>2</sub>MnO<sub>3</sub>  
21  
22  
23 Superstructure. *Adv. Mater.* **2018**, *30*,1707255.  
24  
25  
26
- 27  
28 4. Hwang, J. Y.; Myung, S. T.; Sun, Y. K., Sodium-ion Batteries: Present and  
29  
30  
31 Future. *Chem. Soc. Rev.* **2017**, *46*, 3529-3614.  
32  
33  
34
- 35  
36 5. Hu, Y. S.; Komaba, S.; Forsyth, M.; Johnson, C.; Rojo, T., A New Emerging  
37  
38  
39 Technology: Na-Ion Batteries. *Small Methods* **2019**, *3*, 1900184.  
40  
41
- 42  
43 6. Ebner, M.; Marone, F.; Stampanoni, M.; Wood, V., Visualization and  
44  
45  
46 Quantification of Electrochemical and Mechanical Degradation in Li Ion Batteries.  
47  
48  
49 *Science* **2013**, *342*, 716-720.  
50  
51  
52  
53  
54  
55  
56  
57  
58  
59  
60

- 1  
2  
3  
4 7. Aifantis, K. E.; Huang, T.; Hackney, S. A.; Sarakonsri, T.; Yu, A. S., Capacity  
5  
6  
7 fade in Sn-C nanopowder anodes due to fracture. *J. Power Sources* **2012**, *197*, 246-  
8  
9  
10 252.  
11  
12
- 13  
14 8. Aifantis, K. E.; Hackney, S. A., Mechanical Stability for Nanostructured Sn- and  
15  
16  
17 Si-Based Anodes. *J. Power Sources* **2011**, *196*, 2122-2127.  
18  
19
- 20  
21 9. Aifantis, K. E.; Dempsey, J. P., Stable Crack Growth in Nanostructured Li-  
22  
23  
24 batteries. *J. Power Sources* **2005**, *143*, 203-211.  
25  
26  
27
- 28 10. Xu, J. G.; Deshpande, R. D.; Pan, J.; Cheng, Y. T.; Battaglia, V. S., Electrode  
29  
30  
31 Side Reactions, Capacity Loss and Mechanical Degradation in Lithium-Ion Batteries. *J.*  
32  
33  
34 *Electrochem. Soc.* **2015**, *162*, A2026-A2035.  
35  
36  
37
- 38 11. Aifantis, K. E.; Haycock, M.; Sanders, P.; Hackney, S. A., Fracture of  
39  
40  
41 Nanostructured Sn/C Anodes during Li-insertion. *Mat Sci Eng a-Struct* **2011**, *529*, 55-  
42  
43  
44 61.  
45  
46  
47
- 48 12. McGrogan, F. P.; Raja, S. N.; Chiang, Y. M.; Van Vliet, K. J.,  
49  
50  
51  
52 Electrochemomechanical Fatigue: Decoupling Mechanisms of Fracture- Induced  
53  
54  
55  
56 Performance Degradation in  $\text{Li}_x\text{Mn}_2\text{O}_4$ . *J. Electrochem. Soc.* **2018**, *165*, A2458-A2466.  
57  
58  
59  
60

- 1  
2  
3  
4 13. Qi, Y.; Xu, Q. C.; Van der Ven, A., Chemically Induced Crack Instability When  
5  
6  
7 Electrodes Fracture. *J. Electrochem. Soc.* **2012**, *159*, A1838-A1843.  
8  
9
- 10 14. Hao, X. G.; Lin, X. K.; Lu, W.; Bartlett, B. M., Oxygen Vacancies Lead to Loss of  
11  
12  
13 Domain Order, Particle Fracture, and Rapid Capacity Fade in Lithium Manganospinel  
14  
15  
16 (LiMn<sub>2</sub>O<sub>4</sub>) Batteries. *ACS Appl. Mater. Interfaces* **2014**, *6*, 10849-10857.  
17  
18  
19
- 20 15. Qu, M.; Woodford, W. H.; Maloney, J. M.; Carter, W. C.; Chiang, Y. M.; Van Vliet,  
21  
22  
23 K. J., Nanomechanical Quantification of Elastic, Plastic, and Fracture Properties of  
24  
25  
26 LiCoO<sub>2</sub>. *Adv. Energy Mater.* **2012**, *2*, 940-944.  
27  
28  
29
- 30 16. Yu, Y. S.; Kim, C.; Shapiro, D. A.; Farmand, M.; Qian, D.; Tyliszczak, T.;  
31  
32  
33 Kilcoyne, A. L. D.; Celestre, R.; Marchesini, S.; Joseph, J.; Denes, P.; Warwick, T.;  
34  
35  
36 Strobridge, F. C.; Grey, C. P.; Padmore, H.; Meng, Y. S.; Kostecki, R.; Cabana, J.,  
37  
38  
39 Dependence on Crystal Size of the Nanoscale Chemical Phase Distribution and  
40  
41  
42 Fracture in Li<sub>x</sub>FePO<sub>4</sub>. *Nano Lett.* **2015**, *15*, 4282-4288.  
43  
44  
45
- 46 17. Yan, P. F.; Zheng, J. M.; Gu, M.; Xiao, J.; Zhang, J. G.; Wang, C. M.,  
47  
48  
49 Intragranular Cracking as a Critical Barrier for High-Voltage Usage of Layer-Structured  
50  
51  
52 Cathode for Lithium-Ion Batteries. *Nat. Commun.* **2017**, *8*, 14101.  
53  
54  
55  
56  
57  
58  
59  
60

- 1  
2  
3  
4 18. Xu, B.; Meng, S., Factors Affecting Li Mobility in Spinel  $\text{LiMn}_2\text{O}_4$ -A First-  
5  
6  
7 Principles Study by GGA and GGA Plus U methods. *J. Power Sources* **2010**, *195*,  
8  
9  
10 4971-4976.  
11  
12  
13  
14 19. Wang, D. Y.; Wu, X. D.; Wang, Z. X.; Chen, L. Q., Cracking Causing Cyclic  
15  
16  
17 Instability of  $\text{LiFePO}_4$  Cathode Material. *J. Power Sources* **2005**, *140*, 125-128.  
18  
19  
20  
21 20. Wang, J. W.; Liu, X. H.; Mao, S. X.; Huang, J. Y., Microstructural Evolution of Tin  
22  
23  
24 Nanoparticles during In Situ Sodium Insertion and Extraction. *Nano Lett.* **2012**, *12*,  
25  
26  
27 5897-5902.  
28  
29  
30  
31 21. Gu, M.; Kushima, A.; Shao, Y. Y.; Zhang, J. G.; Liu, J.; Browning, N. D.; Li, J.;  
32  
33  
34 Wang, C. M., Probing the Failure Mechanism of  $\text{SnO}_2$  Nanowires for Sodium-Ion  
35  
36  
37 Batteries. *Nano Lett.* **2013**, *13*, 5203-5211.  
38  
39  
40  
41  
42 22. You, Y.; Wu, X. L.; Yin, Y. X.; Guo, Y. G., High-Quality Prussian Blue Crystals as  
43  
44  
45 Superior Cathode Materials for Room-Temperature Sodium-Ion Batteries. *Energy*  
46  
47  
48 *Environ. Sci.* **2014**, *7*, 1643-1647.  
49  
50  
51  
52  
53  
54  
55  
56  
57  
58  
59  
60

- 1  
2  
3  
4 23. Wang, L.; Lu, Y. H.; Liu, J.; Xu, M. W.; Cheng, J. G.; Zhang, D. W.; Goodenough,  
5  
6  
7 J. B., A Superior Low-Cost Cathode for a Na-Ion Battery. *Angew Chem Int Edit* **2013**,  
8  
9  
10 *52*, 1964-1967.  
11  
12  
13  
14 24. Lu, Y. H.; Wang, L.; Cheng, J. G.; Goodenough, J. B., Prussian Blue: a New  
15  
16  
17 Framework of Electrode Materials for Sodium Batteries. *Chem. Commun.* **2012**, *48*,  
18  
19  
20  
21 6544-6546.  
22  
23  
24 25. Xiao, P. H.; Song, J.; Wang, L.; Goodenough, J. B.; Henkelman, G., Theoretical  
25  
26  
27 Study of the Structural Evolution of a  $\text{Na}_2\text{FeMn}(\text{CN})_6$  Cathode upon Na Intercalation.  
28  
29  
30  
31 *Chem. Mater.* **2015**, *27*, 3763-3768.  
32  
33  
34  
35 26. Song, J.; Wang, L.; Lu, Y. H.; Liu, J.; Guo, B. K.; Xiao, P. H.; Lee, J. J.; Yang, X.  
36  
37  
38 Q.; Henkelman, G.; Goodenough, J. B., Removal of Interstitial  $\text{H}_2\text{O}$  in  
39  
40  
41 Hexacyanometallates for a Superior Cathode of a Sodium-Ion Battery. *J. Am. Chem.*  
42  
43  
44  
45 *Soc.* **2015**, *137*, 2658-2664.  
46  
47  
48  
49 27. Pan, H. L.; Hu, Y. S.; Chen, L. Q., Room-Temperature Stationary Sodium-Ion  
50  
51  
52 Batteries For Large-Scale Electric Energy Storage. *Energy Environ. Sci.* **2013**, *6*, 2338-  
53  
54  
55  
56 2360.  
57  
58  
59  
60

- 1  
2  
3  
4 28. Matsuda, T.; Takachi, M.; Moritomo, Y., A Sodium Manganese Ferrocyanide Thin  
5  
6  
7 Film For Na-Ion Batteries. *Chem. Commun.* **2013**, *49*, 2750-2752.  
8  
9
- 10 29. Gao, H. C.; Xin, S.; Xue, L. G.; Goodenough, J. B., Stabilizing a High-Energy-  
11  
12  
13 Density Rechargeable Sodium Battery with a Solid Electrolyte. *Chem-US* **2018**, *4*, 833-  
14  
15  
16  
17 844.  
18  
19
- 20 30. Yang, D. Z.; Xu, J.; Liao, X. Z.; He, Y. S.; Liu, H. M.; Ma, Z. F., Structure  
21  
22  
23  
24 Optimization of Prussian Blue Analogue Cathode Materials for Advanced Sodium Ion  
25  
26  
27  
28 Batteries. *Chem. Commun.* **2014**, *50*, 13377-13380.  
29  
30
- 31 31. Moritomo, Y.; Urase, S.; Shibata, T., Enhanced Battery Performance in  
32  
33  
34  
35 Manganese Hexacyanoferrate by Partial Substitution. *Electrochim. Acta* **2016**, *210*, 963-  
36  
37  
38  
39 969.  
40  
41
- 42 32. Moritomo, Y.; Wakaume, K.; Takachi, M.; Zhu, X. H.; Kamioka, H., Li<sup>+</sup>  
43  
44  
45  
46 Intercalation of Manganese Ferrocyanide as Investigated by In situ Valence-Differential  
47  
48  
49 Absorption Spectroscopy. *J. Phys. Soc. Jpn.* **2013**, *82*, 094710.  
50  
51
- 52 33. Tang, K.; Yu, X. Q.; Sun, J. P.; Li, H.; Huang, X. J., Kinetic analysis on LiFePO<sub>4</sub>  
53  
54  
55  
56 thin films by CV, GITT, and EIS. *Electrochim. Acta* **2011**, *56*, 4869-4875.  
57  
58  
59  
60

- 1  
2  
3  
4 34. Rui, X. H.; Ding, N.; Liu, J.; Li, C.; Chen, C. H., Analysis of the Chemical  
5  
6  
7 Diffusion Coefficient of Lithium Ions in  $\text{Li}_3\text{V}_2(\text{PO}_4)_3$  Cathode Material. *Electrochim. Acta*  
8  
9  
10 **2010**, *55*, 2384-2390.  
11  
12  
13  
14 35. Rethore, J.; Zheng, H.; Li, H.; Li, J. J.; Aifantis, K. E., A Multiphysics Model that  
15  
16  
17 can Capture Crack Patterns in Si Thin Films Based on Their Microstructure. *J. Power*  
18  
19  
20 *Sources* **2018**, *400*, 383-391.  
21  
22  
23  
24 36. Zhao, Y.; Adair, K. R.; Sun, X. L., Recent Developments and Insights into the  
25  
26  
27 Understanding of Na Metal Anodes for Na-Metal Batteries. *Energy Environ. Sci.* **2018**,  
28  
29  
30 *11*, 2673-2695.  
31  
32  
33  
34 37. Liu, T.; Zhang, Y.; Jiang, Z.; Zeng, X.; Ji, J.; Li, Z.; Gao, X.; Sun, M.; Lin, Z.; Ling,  
35  
36  
37 M.; Zheng, J.; Liang, C., Exploring Competitive Features of Stationary Sodium Ion  
38  
39  
40 Batteries for Electrochemical Energy Storage. *Energy Environ. Sci.* **2019**, *12*, 1512-  
41  
42  
43  
44 1533.  
45  
46  
47  
48 38. Jache, B.; Adelhelm, P., Use of Graphite as a Highly Reversible Electrode with  
49  
50  
51 Superior Cycle Life for Sodium-Ion Batteries by Making Use of Co-Intercalation  
52  
53  
54  
55 Phenomena. *Angew Chem Int Edit* **2014**, *53*, 10169-10173.  
56  
57  
58  
59  
60

1  
2  
3  
4  
5  
6  
7  
8  
9  
10  
11  
12  
13  
14  
15  
16  
17  
18  
19  
20  
21  
22  
23  
24  
25  
26  
27  
28  
29  
30  
31  
32  
33  
34  
35  
36  
37  
38  
39  
40  
41  
42  
43  
44  
45  
46  
47  
48  
49  
50  
51  
52  
53  
54  
55  
56  
57  
58  
59  
60